Time-dependent triggered afterslip following the 1989 Loma Prieta earthquake

Paul Segall

Department of Geophysics, Stanford University, Stanford, California

Roland Bürgmann

Department of Geology and Geophysics, University of California, Berkeley

Mark Matthews

Walden Consulting, Wayland, Massachusetts

Abstract. We employ a modified version of the Network Inversion Filter to investigate time-dependent slip following the 1989 Loma Prieta earthquake. Previous analysis of Global Positioning System (GPS) and leveling data suggests afterslip on the Loma Prieta rupture as well as aseismic slip on a thrust fault northeast of the San Andreas fault which we identify with the Foothills thrust belt. We analyzed 173 daily GPS solution files at 62 stations collected from 1989.8 to 1998.3 (a total of 1,134 three-dimensional relative baseline determinations). The observed position changes are assumed to result from secular deformation, random benchmark motions, and temporally varying fault slip. The data reveal temporal variations in slip rate but poorly resolve spatial variations in fault slip. The amount of temporal smoothing is estimated by maximum likelihood. Conditional on this estimate, reverse slip on the Foothills thrust decays from 45 ± 12 mm/yr immediately after the earthquake to zero by 1992. Reverse slip on the Loma Prieta rupture surface decays from 57 ± 11 mm/yr to zero by 1994. Right-lateral slip on the Loma Prieta rupture surface decays monotonically from 30 ± 10 mm/yr to zero by 1994. These results suggest that (1) triggered afterslip can occur off the main rupture zone on adjacent faults, (2) shallow afterslip dominated the postseismic deformation for the 8 years following the earthquake, and (3) postseismic slip on the Foothills thrust may account for a significant portion of its total slip budget.

1. Introduction

Geodetic measurements have revealed a great deal about the geometry and slip distribution during earthquakes [e.g., *Árnadóttir and Segall*, 1994; *Hudnut et al.*, 1994; *Bennett et al.*, 1995; *Murray et al.*, 1996]. Much less is known about transient aseismic slip associated with earthquakes. There is considerable evidence of afterslip following some earthquakes [e.g., *Smith and Wyss*, 1968; *Prescott et al.*, 1984; *Bilham*, 1989; *Shen et al.*, 1994; *Savage and Svarc*, 1997]. In many cases the moment released by slow afterslip is substantially greater than that released by aftershocks.

Our knowledge of transient aseismic slip is rather limited because the data are restricted to geodetic survey measurements and strain meters, and until recently, these networks have been spatially and/or temporally

limited. Yet there are a number of important reasons for studying aseismic slip. Aseismic slip can have a strong influence on the moment budget of faults. The central creeping zone of the San Andreas fault is the most obvious example of this phenomenon. More recently, *Heki et al.* [1997] showed that afterslip following a subduction zone earthquake off the Sanriku coast of Japan represented moment comparable to that released in the mainshock. Afterslip redistributes stress in the crust, and this stress redistribution can be important in the occurrence of future earthquakes. Finally, improved imaging of afterslip may help to constrain fault zone constitutive laws.

There are a number of questions related to earthquake afterslip that have yet to be addressed. We know that coseismic slip distributions are often quite spatially heterogeneous [e.g., *Árnadóttir and Segall*, 1994; *Wald and Heaton*, 1994]. Does postseismic slip represent continued sliding in areas of peak slip, or does it tend to fill in the areas of low coseismic slip? Is postseismic fault displacement restricted to shear offset in the

plane of the fault, or is there evidence for collapse of dilatancy created during the earthquake [e.g., *Savage et al.,* 1994]. If there is fault-normal motion, does it occur in areas of high coseismic dilatancy or in areas of postseismic slip? In order to address these questions, we require the data and inverse methods that allow for detailed imaging of postseismic processes.

This paper represents an initial attempt at using Global Positioning System (GPS) data to map the spatial and temporal distribution of afterslip following a $M7$ earthquake. We focus on the 1989 Loma Prieta earthquake because there now exists an extensive set of 8 years of postearthquake GPS measurements. While we initially suspected that viscous-like relaxation of the lower crust would be the dominant postseismic process, evidence from the Loma Prieta earthquake clearly shows that brittle response of the upper crust dominates the observable deformation in the decade following the mainshock [*Bürgmann et al.,* 1997; *Pollitz et al.,* 1998].

2. Data

In this study we employ all GPS data collected in the Loma Prieta region, from immediately after the earthquake (1989.80) until 1998.27. The data were collected by a number of different groups and agencies including the U.S. Geological Survey, the National Geodetic Survey, Stanford University, and University of California, Davis. Field methods and data processing are described in detail by *Bürgmann et al.* [1997] for all data collected up to 1994. Data collected from 1995 to 1998 were analyzed with the same processing methods, using the Bernese (versions 3.5 and 4.0) [*Rothacher et al.,* 1996] GPS processing software and fixed International GPS Service (IGS) precise orbits [*Beutler et al.,* 1999]. Two fiducial stations (Quincy and Mojave) were constrained to their ITRF-92 (International Terrestrial Reference Frame) positions at each data epoch.

The data set is quite heterogeneous, in the sense that different subnetworks were surveyed by different groups at different times, and more stations were continuously added to the network in later occupations. Nearby permanent GPS sites did not exist in the region until September 1991 when two stations were installed near the Hayward fault [*King et al.,* 1995]. Data from the permanent site SUAA at Stanford University, part of the Bay Area Regional Deformation (BARD) network, were included in the solutions beginning in 1994. While many of the surveys included a station on Loma Prieta (LP1), this site was not included in all surveys. In fact, no single local station was occupied during each survey. Despite this, the data set is quite extensive. The network consists of 62 stations (Figure 1), and there are a total of 173 daily GPS position solutions. A total of 1,134 three-dimensional position determinations leads to a data vector with 2,883 relative baseline components. Notice, however, that the average station was occupied only $\sim$ 18 times, and only 11 sites were sur-

veyed more than 25 times (Figure 1). LP1, the most frequently occupied station near the epicentral region, was observed 64 times. Thus we anticipate that we will only be able to recover the general characteristics of the postseismic transient motions.

3. Method

We employ a modified form of the Network Inversion Filter (NIF) [*Matthews and Segall,* 1988; *Segall and Matthews,* 1997] to analyze the GPS observations. Before describing the details of the NIF, we contrast the filtering approach with the more standard analysis approach. The most common method is to assume a parametric form for the time dependence of the deformation, typically logarithmic or exponential. The time series are individually fit to the parametric equation, and the computed parameters (e.g., the slope, net offset, or cumulative displacement) are then inverted for the geometry of the fault or the distribution of slip on the fault.

In contrast the Network Inversion Filter does not assume a particular parametric form for the time dependence of the deformation. The filter is allowed (within some bounds) to find whatever time dependence is necessary to fit the data. Secondly, the spatial and temporal variations are modeled simultaneously using the observed GPS derived positions and covariances. Finally, random local benchmark motions are explicitly modeled. The fact that the filter analyzes data from the full network simultaneously allows the algorithm to distinguish between temporal variations that are local to a single station, and thus unlikely to be tectonic, from temporal variations that are coherent across the geodetic network, and thus likely to represent time-varying fault motion. Spatially and temporally correlated noise processes could, however, be mismodeled as crustal deformation.

We now discuss the differences between this implementation of the Network Inversion Filter and that described by *Segall and Matthews* [1997]. Because the data are irregularly sampled in time, and in particular most stations were not observed immediately following the earthquake, we need to consider the vector positions of the GPS stations rather than displacements. That is, we can not difference all observations to the first measurement epoch, since all sites were not observed at that, or any, particular time. We actually model relative baseline vectors, by subtracting the position of one arbitrary site, from the other simultaneously observed positions. The reference site does not need to be the same from day to day, nor does it need to be stationary, since the relative motion is modeled. This procedure removes any errors in the absolute position determinations due to translational biases in the reference frame. It does not, however, remove rotational or scale biases that may occur. This is particularly important in the early data collected shortly after the 1989
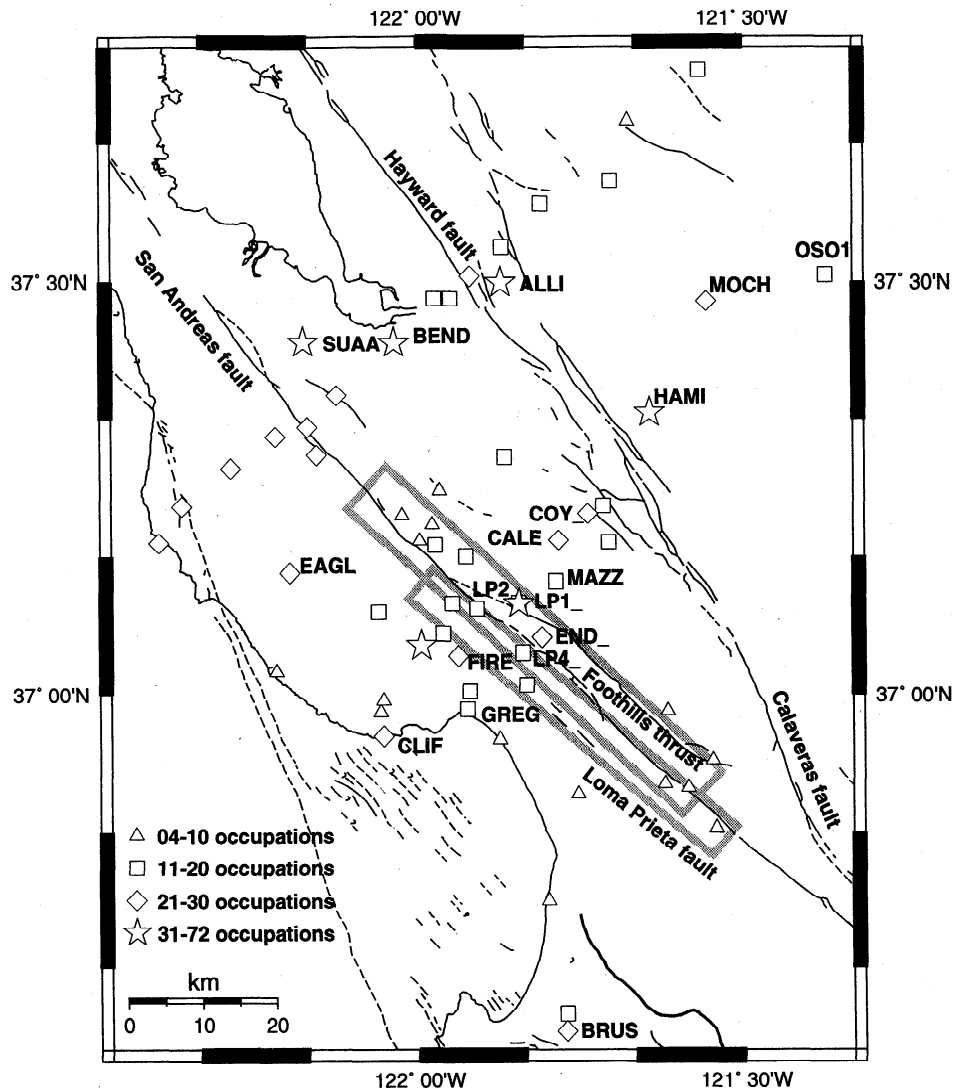
Figure 1. Network of Global Positioning System (GPS) sites that were measured following the 1989 Loma Prieta earthquake. The different symbols indicate the number of daily station occupations.

earthquake when GPS tracking networks were much less extensive than they are today.

The observed coordinates at time t, $\mathbf{x}(t)$, equal the positions at some reference epoch t_0, $\mathbf{x}(t_0)$, plus any motion that occurs between t and t_0, and observation errors,

$$\mathbf{x}_r(t) \quad - \quad \mathbf{v}_r^{\text{sec}}(\mathbf{x})(t - t_0) \ = \ \mathbf{x}_r(t_0) \ +$$
$$+ \int_A s_p(\boldsymbol{\xi}, t - t_0) G_{pq}^r(\mathbf{x}, \boldsymbol{\xi}) \mathbf{n}_q(\boldsymbol{\xi}) dA(\boldsymbol{\xi})$$
$$+ \mathcal{L}(\mathbf{x}, t - t_0) \ + \ \boldsymbol{\epsilon}. \tag{1}$$

The first term on the left-hand side of (1) is the observed position at time t. The second term on the left-hand side accounts for the expected secular motion at velocity $\mathbf{v}_r^{\text{sec}}(\mathbf{x})$ that would have accumulated between time t_0 and time t had no earthquake occurred. Here we use the interseismic model developed by *Bürgmann et al.* [1997]

based on 20 years of geodolite observations collected by the U.S. Geological Survey (USGS) prior to the 1989 earthquake. The second term on the right-hand side of (1) represents motion due to slip $\mathbf{s}(\boldsymbol{\xi}, t - t_0)$ on one or more fault surfaces A, which accumulates following the earthquake. Here, $p, q, r = 1, 2, 3$, summation on repeated indices is implied, and $\mathbf{n}_q(\boldsymbol{\xi})$ is the unit normal to the fault surface $A(\boldsymbol{\xi})$. The kernels $G_{pq}^r(\mathbf{x}, \boldsymbol{\xi})$ are the elastostatic Green's functions for dislocations [e.g., *Aki and Richards*, 1980] in a homogeneous, isotropic, elastic half-space [e.g., *Okada*, 1985]; that is, they relate unit slip in the p direction on a fault with normal in the q direction to displacement in the r direction. The third term on the right-hand side, $\mathcal{L}(\mathbf{x}, t - t_0)$, represents local benchmark motions due to surficial processes. We take these spatially incoherent motions to follow a Brownian random walk process [*Wyatt*, 1982, 1989; *Langbein and Johnson*, 1997] with scale parameter τ (units of

length/time$^{1/2}$). The final term represents the observation errors, which are taken to be normally distributed with covariance matrix $\sigma^2\Sigma$, where Σ is the formal covariance matrix derived from the GPS analysis and σ^2 is an unknown scalar factor, which accounts for the difference between formal errors and the observed repeatability in the GPS data [e.g., *Larson et al.*, 1991]. The scaling is required because the GPS analysis software does not completely account for some error sources, including multipath, nonuniform variations in tropospheric delay, unmodeled variations in antenna phase patterns, etc. In detail, Σ is already scaled as in the work of *Bürgmann et al.* [1997] to account for differences observed between solutions with computed orbits (prior to mid-1991) and those with fixed IGS orbits.

The unknown slip is taken to be a linear combination of spatial basis functions, $\mathcal{B}(\mathbf{x})$, in which the coefficients are time varying, $s(\mathbf{x}, t) = \sum_{k=1}^{M} c_k(t)\mathcal{B}_k(\mathbf{x})$. The temporal variation is modeled nonparametrically, by taking the slip accelerations to be random Gaussian increments. The coefficients $c_k(t)$ are thus composed of a steady velocity v_k and an integrated random walk $W_k(t)$ with scale parameter α^2 (units of length^2/time^3):

$$c_k(t) = v_k t + W_k(t). \qquad (2)$$

$W_k(t)$ is the integral of a random walk process, or twice integrated formal white noise with variance α^2. In the limit $\alpha^2 \to 0$ the estimated slip rate is constant, equal to v_k, whereas with increasing α^2 the slip rate becomes more temporally variable in order to improve the fit to the data. Several examples based on fits to synthetic data are given by *Segall and Matthews* [1997].

The Network Inversion Filter is a linear method that assumes that the geometry of the active structures is known. In this analysis we employ the two dislocation surfaces estimated from the data by *Bürgmann et al.* [1997]. This study used the average rates of change on the GPS baselines from 1989 to 1994, as well as vertical displacement rates from repeated leveling, to infer the position of the active structures following the 1989 earthquake. Bürgmann et al. found that two dislocation surfaces were required to fit the data. The first dislocation corresponds to the Loma Prieta rupture surface. The second dislocation is a southwest dipping reverse fault located in the Foothills thrust belt northeast of the San Andreas. The reverse fault is required in order to explain convergence normal to the trend of the San Andreas observed in the postseismic GPS data [*Savage et al.*, 1994] and uplift of the hanging wall of the Foothills thrust [*Bürgmann et al.*, 1997].
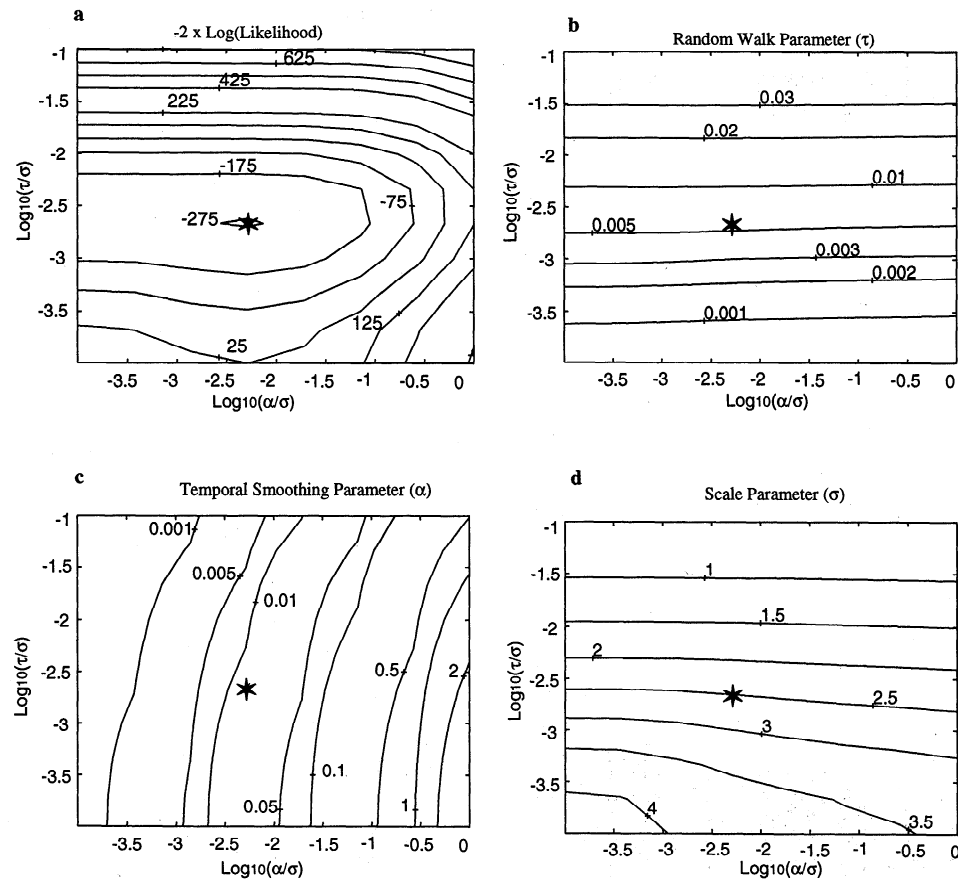
4. Analysis

The first step in the analysis is to estimate the slip acceleration parameter α and the scale of the random walk motions τ. These parameters can be estimated directly from the data using maximum likelihood techniques

[*Segall and Matthews*, 1997]. The available GPS data, however, are sparsely and heterogeneously sampled. We analyzed a frequently measured 16 station subset of the data, including the Loma Prieta profile (stations CLIF, GREG,FIRE, END, LP1, LP2, LP4, MAZZ, CALE, COY, MOCH, OSO1) as well as the Monitor network (stations BRUS, EAGL, HAMI, ALLI). The mean number of observations in the subset is 21, and the maximum (at LP1) is 46. The $-2\times$ log(likelihood) surface is shown in Figure 2a as a function of α/σ and τ/σ. The maximum likelihood point corresponding to the minimum of the $-2\times$ log(likelihood) is given by $\tau = 0.005$ m/yr$^{1/2}$, $\alpha = 0.013$ m/yr$^{3/2}$, and $\sigma = 2.4$.

As can be seen from Figure 2b, the random walk parameter τ is nearly independent of the value of α, demonstrating that the Network Inversion Filter is capable of distinguishing between local benchmark motion and time-dependent fault slip. Note that we do not estimate different values of τ at each site, although it is almost certain that some sites are more subject to local monument instability than others. The reason for this is simply that with only 21 observations (on average) there are insufficient data to obtain a reliable estimate of the random walk scale at each station.

Our estimate of the average random walk scale parameter, $\tau = 5$ mm/yr$^{1/2}$, is somewhat higher than estimates based on much greater amounts of laser ranging data elsewhere in California. *Langbein and Johnson* [1997] estimated τ, ranging from 4 mm/yr$^{1/2}$ at "unstable" sites to 1 mm/yr$^{1/2}$ for "stable" sites. Note that the laser retroreflectors extend well above the ground surface, in contrast to the standard brass tablets mounted on steel rods that are used in GPS geodetic studies. More importantly, there are almost certainly time dependent errors intrinsic to GPS that are not present in laser ranging data. The difference between our estimate and those of Langbein and Johnson is at least partly due to the paucity of measurements in the post Loma Prieta GPS data set. With somewhat over 300 total observations (in the maximum likelihood analysis) there may not be sufficient data to yield a robust measure of the random walk variance. Given the nonlinear nature of the estimation, it is difficult to determine a rigorous estimate of the uncertainty in τ. Figure 3, which shows the variation in the likelihood as a function of τ for α fixed at the maximum likelihood estimate, emphasizes that the minimum in the $-2\times$log(likelihood) is reasonably broad, suggesting that τ is not tightly constrained. (Note that the slightly larger maximum likelihood estimate of τ is due to the finer sampling in Figure 3 compared to Figure 2b). It is also possible that antenna setup errors contribute to the somewhat larger than expected estimate of the random walk parameter. We tested omitting the vertical component from the maximum likelihood calculation and analyzing only data from 1993 onward. Neither had a significant effect. Finally, it is also possible that our simplified model does

Figure 2. Maximum likelihood analysis of variance parameters. (a) Minus twice the logarithm of the likelihood surface as a function of $log_{10}(\alpha/\sigma)$ and $log_{10}(\tau/\sigma)$. The maximum likelihood value (the minimum point on the surface) is indicated by an asterisk. (b) Random walk parameter τ as a function of $log_{10}(\alpha/\sigma)$ and $log_{10}(\tau/\sigma)$. The maximum likelihood value is indicated by an asterisk. Note that the estimate of τ is nearly independent of α. (c) Temporal smoothing parameter α as a function of $log_{10}(\alpha/\sigma)$ and $log_{10}(\tau/\sigma)$. The maximum likelihood value is indicated by an asterisk. Note that the estimate of α is only weakly dependent on τ. (d) Data covariance scale factor σ as a function of $log_{10}(\alpha/\sigma)$ and $log_{10}(\tau/\sigma)$. The maximum likelihood value is indicated by an asterisk.

not adequately describe the physics of postseismic deformation, thus artificially increasing the estimate of τ. The fact that we obtain estimates within a factor of 2 of those of Langbein and Johnson, who used vastly more data, is encouraging. For most of the remaining analysis we will assume τ in the range of 2-3 mm/yr$^{1/2}$. We show below that small changes in τ lead to insignificant changes in the estimates of fault slip rate.

Figures 2c and 2d show the values of α and σ also as a function of the ratios α/σ and τ/σ. As can be seen from Figure 2c, the estimated value of the temporal smoothing parameter α is only weakly dependent on the estimated ratio τ/σ. Figure 4 shows the variation in the likelihood as a function of the temporal smoothing parameter for two different values of τ. It is clear from Figure 4 that the maximum likelihood estimate of α does not change significantly for a factor of 2 change in τ.

We also examined a larger subset of the data which included sites more distant from the Loma Prieta rupture zone. This data yielded a somewhat smaller value of α. It makes sense that the larger network yields estimates that are more nearly steady state than does the smaller network which is localized to the Loma Prieta rupture zone. From visual examination of the data time series [*Savage et al.*, 1994; *Bürgmann et al.*, 1997] it is apparent that stations closest to the rupture zone show more evidence of temporal variability. In fact, *Bürgmann et al.* [1997] found no significant postseismic transient motion at distances greater than ~ 20 km from the coseismic rupture zone. Thus we would expect the more localized Loma Prieta subnetwork to correlate with somewhat larger values of the acceleration parameter α.

The nonzero estimate of the acceleration parameter α indicates that the data record a transient deforma-
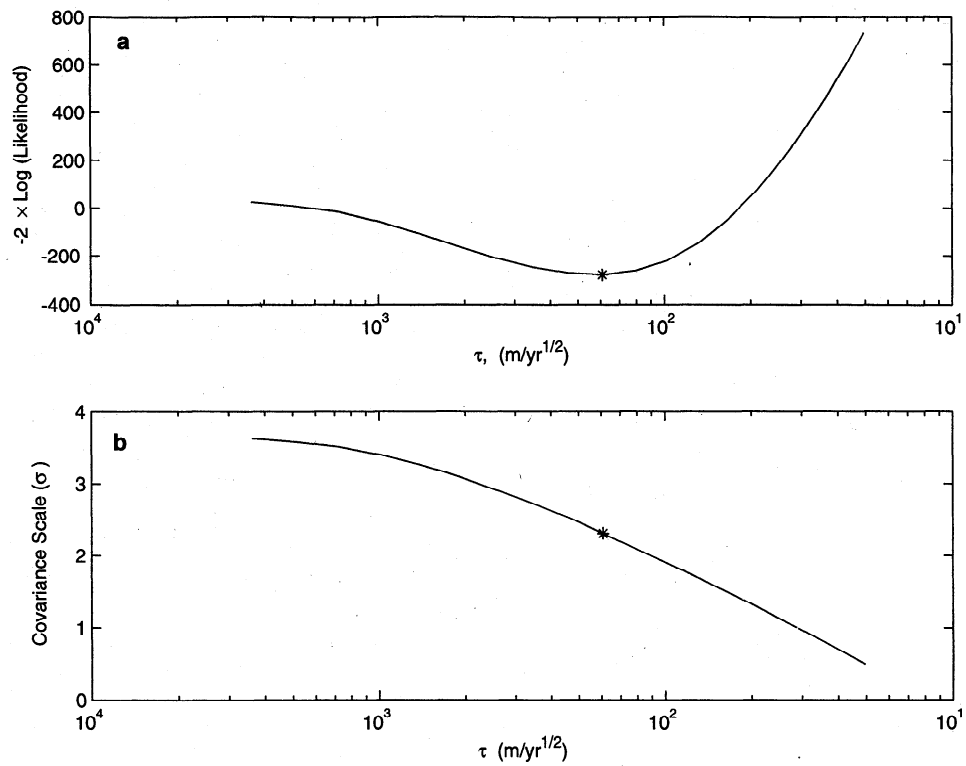
Figure 3. (a) Minus twice the logarithm of the likelihood as a function of τ, with α fixed at the maximum likelihood value. The maximum likelihood estimate of τ is indicated by an asterisk. (b) Data covariance scale factor σ as a function of τ. The maximum likelihood estimate is indicated by an asterisk.
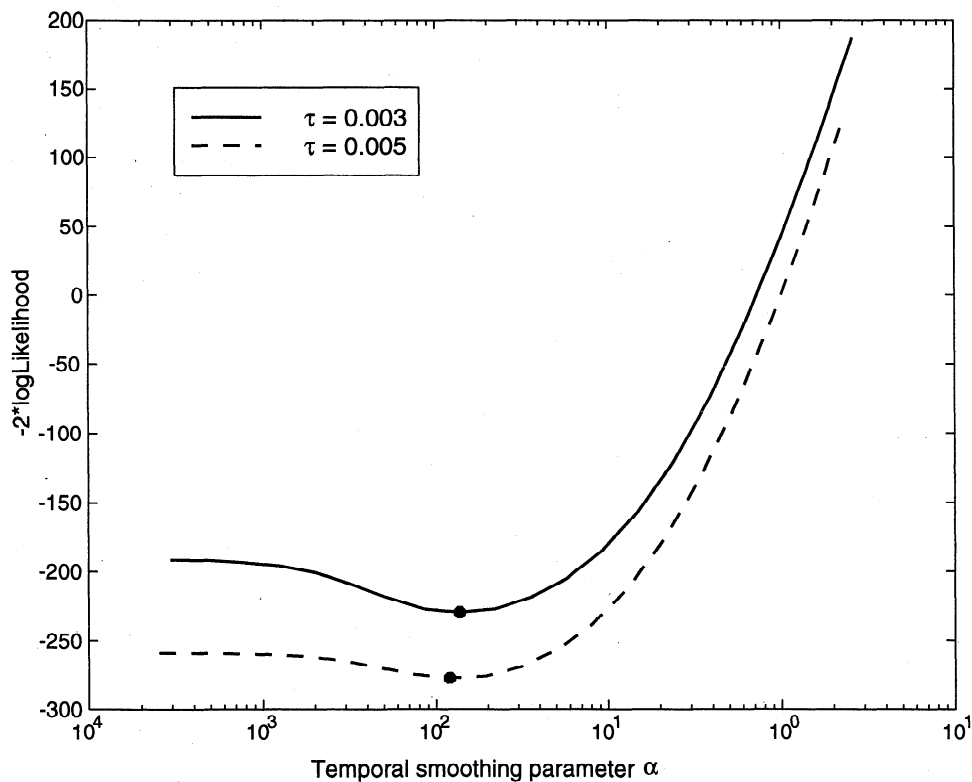
Figure 4. Minus twice the logarithm of the likelihood as a function of the temporal smoothing parameter α for two different values of the random walk scale τ. The maximum likelihood estimates are indicated by circles.
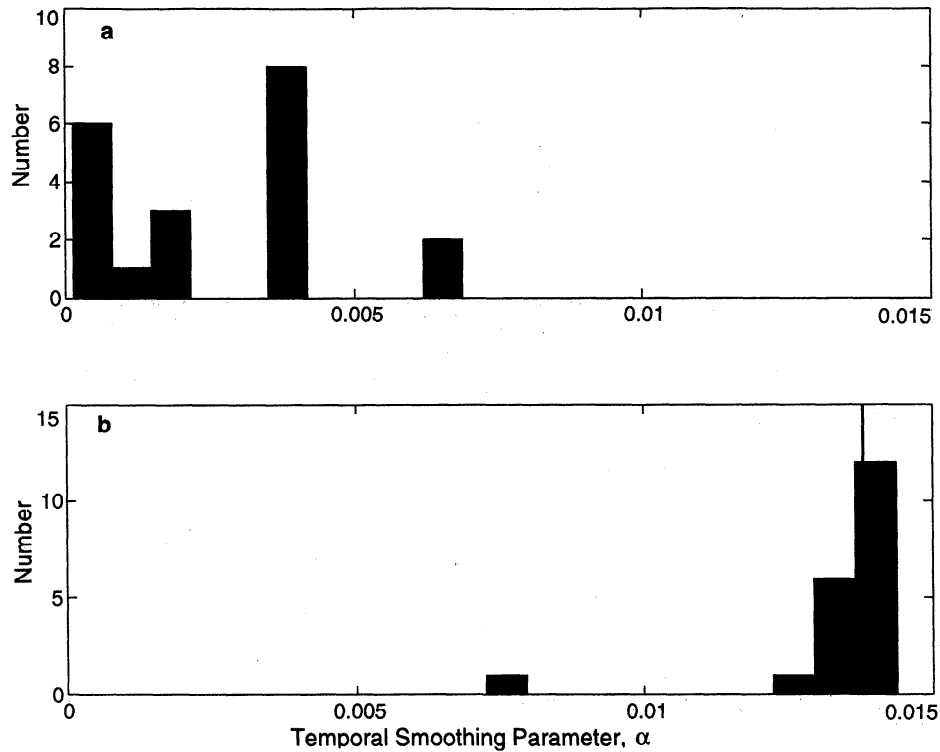
Figure 5. Monte Carlo simulations of temporal smoothing parameter α. (a) Histogram of estimated values from steady state ($\alpha = 0$) simulation. (b) Histogram of estimated values from simulation with $\alpha = 0.013$. The vertical line marks the true value of α. The maximum estimate in Figure 5a is less than the minimum in Figure 5b.

tion process. (Recall that a steady state process corresponds to $\alpha = 0$.) We can test the significance of the nonzero α using the loglikelihood test of *Matthews* [1991]. This test compares the loglikelihood of the full model at the maximum likelihood point, L_{ml}, with the likelihood when α is constrained to be zero, and only τ is estimated from the data, L_0. For this data set, $L_{ml} = 139.5$ and $L_0 = 131.6$. This gives a likelihood ratio statistic of $2(L_{ml} - L_0) = 15.9$, which should follow a χ^2 distribution with one degree of freedom. A value this large is extremely unlikely, suggesting that we can reject the steady-state hypothesis ($\alpha = 0$) with great confidence. It should be noted, however, that allowing nonzero α in fact adds more than a single degree of freedom, since the slip rate may vary at each epoch.

An alternate approach is to use Monte Carlo procedures to test the hypothesis that α is nonzero. We first generated synthetic data according to

$$\hat{x}_r(t) = v_r^{sec}(\mathbf{x})(t - t_0) + \hat{x}_r(t_0)$$

$$+ \int_A \hat{s}_p(\boldsymbol{\xi}, t - t_0)G_{pq}^r(\mathbf{x}, \boldsymbol{\xi})n_q(\boldsymbol{\xi})dA(\boldsymbol{\xi})$$

$$+ \mathcal{L}(\mathbf{x}, t - t_0) + \epsilon, \qquad (3)$$

where $\hat{x}_r(t_0)$ is the estimated position at the reference epoch and is returned directly from the Kalman Filter.
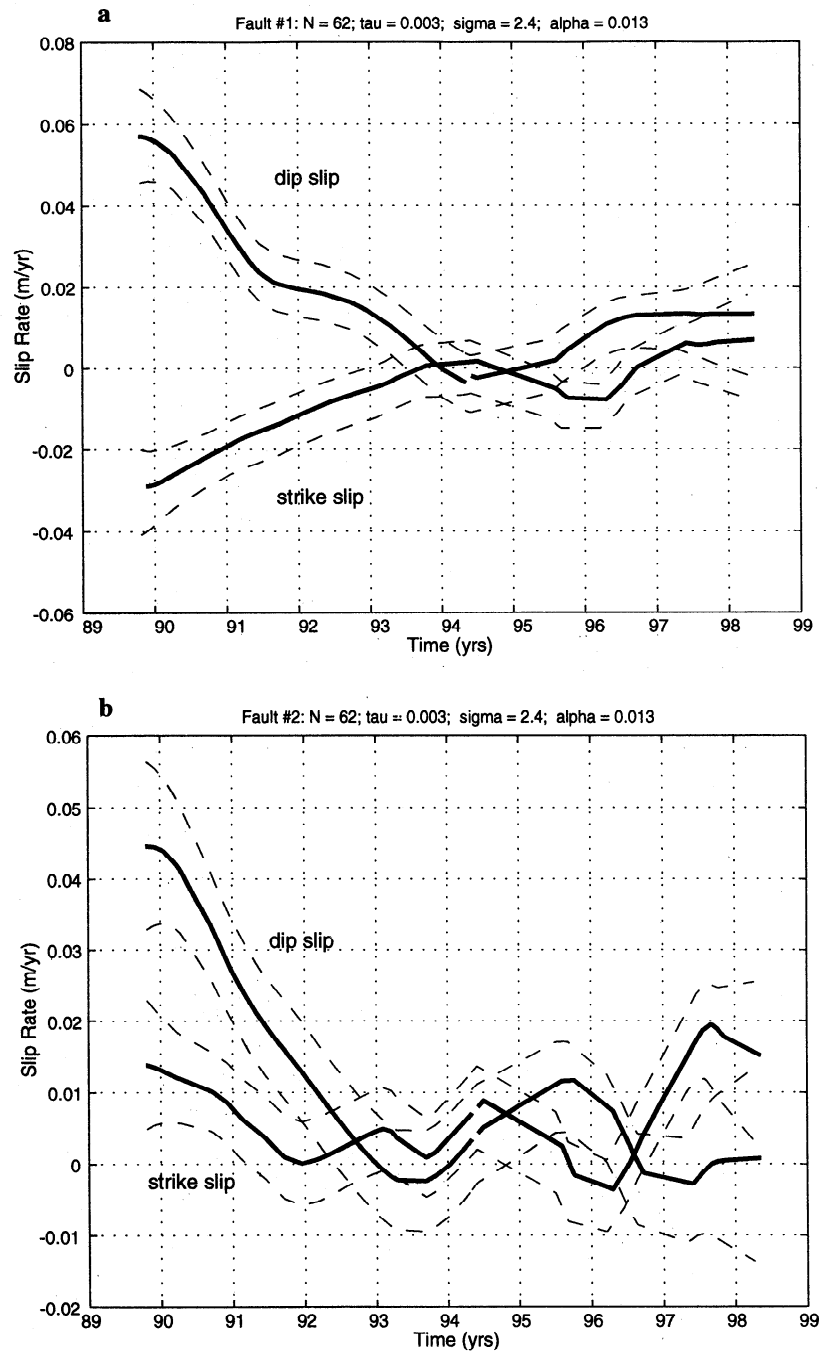
The estimated fault slip $\hat{s}_p(\boldsymbol{\xi}, t - t_0)$ is reconstructed from the estimated basis function coefficients,

$$\hat{s}_p(\boldsymbol{\xi}, t - t_0) = \sum_{k=1}^{M} \hat{c}_{pk}(t - t_0)\mathcal{B}_{pk}(\boldsymbol{\xi}), \qquad (4)$$

where the subscript p refers to the component of slip (strike-slip or dip-slip) and the subscript k refers to the component in the expansion of the slip in the basis functions $\mathcal{B}(\boldsymbol{\xi})$. The coefficients $\hat{c}_{pk}$ are returned from the Kalman Filter.

Random walk was added with scale parameter $\tau = 3$ mm/yr$^{1/2}$. Measurement error was simulated to have the covariance structure of the actual observations at each time step. Conceptually, the data vector at each epoch was normalized by multiplying by the inverse square root of the data covariance matrix. Following this, random normal variates were added, and the data vector was rescaled by multiplying by the square root of the covariance matrix. Mathematically, this amounts to $\mathbf{d}^* = \mathbf{d} + \Upsilon\mathbf{e}$, where $\mathbf{d}^*$ is the simulated data, $\mathbf{e}$ are random variables with unit variance, and Υ is the square root of the data covariance.

We ran two groups of 20 simulations each, estimating α by maximum likelihood for each simulation. In the first group, α was set to zero, simulating a steady state process. The Monte Carlo estimates $\hat{\alpha}^{MC}$ are shown in

a

Fault #1: N = 62; tau = 0.003; sigma = 2.4; alpha = 0.013

[Figure: panel a — Slip Rate (m/yr) vs Time (yrs), with curves labeled "dip slip" and "strike slip"]

b

Fault #2: N = 62; tau = 0.003; sigma = 2.4; alpha = 0.013

[Figure: panel b — Slip Rate (m/yr) vs Time (yrs), with curves labeled "dip slip" and "strike slip"]

Figure 6. Estimated slip rate as a function of time. (a) Slip rate on the Loma Prieta fault. Positive dip slip is thrust, and right-lateral strike slip is negative. (b) Slip rate on the Foothills thrust fault. Dashed lines indicate plus and minus one standard deviation bounds.

Figure 5a. In the second set of 20 simulations, α was set to the maximum likelihood estimate for the actual data, $\alpha = 0.013$. That is, the signal component of the simulated data matched the temporal variability of the observations. These estimates $\hat{\alpha}^{MC}$ are shown in Figure 5b, and are always greater than the maximum estimate in Figure 5a. This strongly suggests that we are unlikely to estimate a value of $\alpha = 0.013$ if the underlying process was truly steady-state. We thus confidently reject the steady-state model.

5. Temporally Variable – Spatially Uniform Slip Results

Given the above estimates of the random walk parameter τ and the acceleration variance α, we are in a position to estimate the temporal variability of the slip from the full GPS data set. As discussed in section 2, this involves 173 daily GPS solution files (and associated covariance matrices) between 1989.80 and 1998.27.

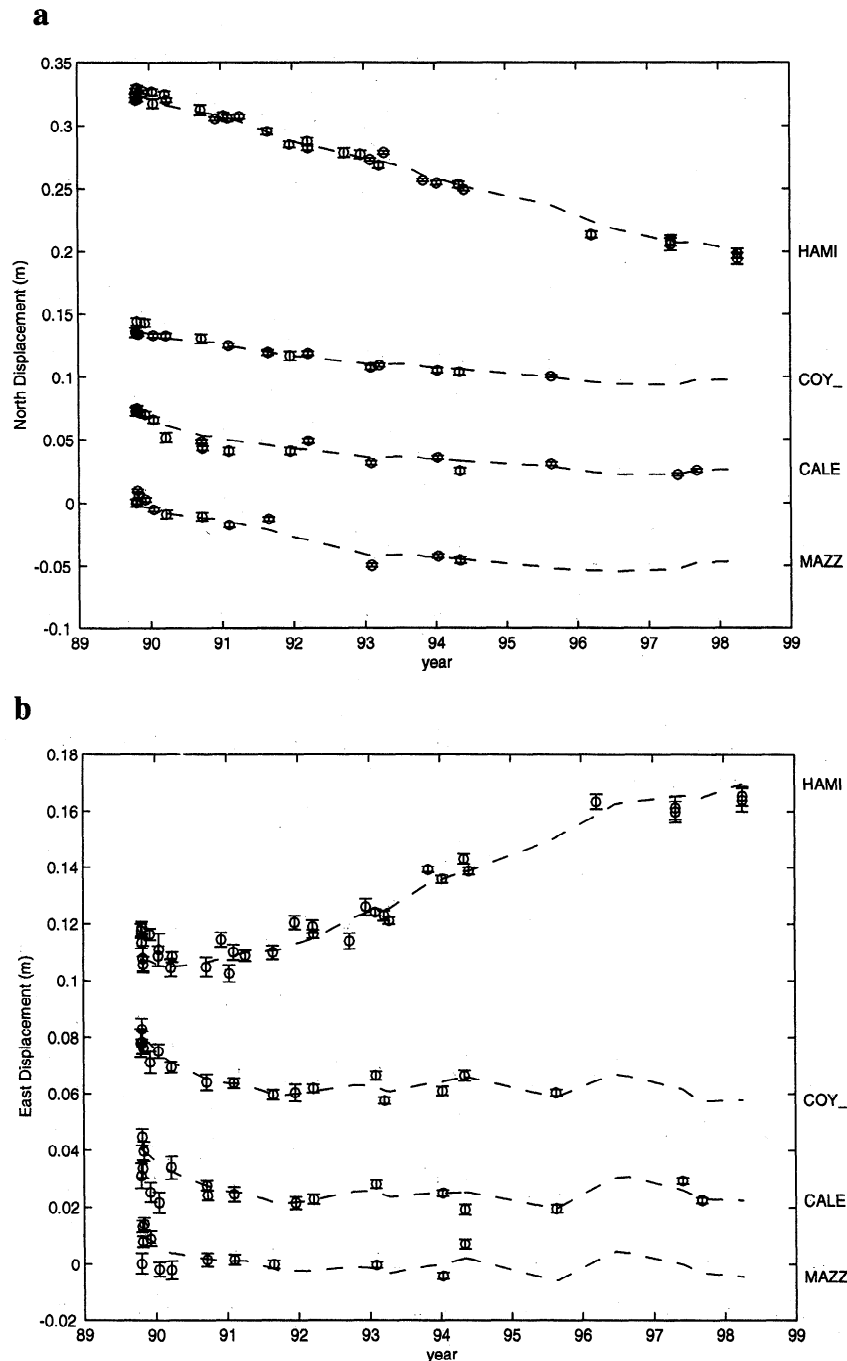With reference to equation (1) the estimated param-

a

b
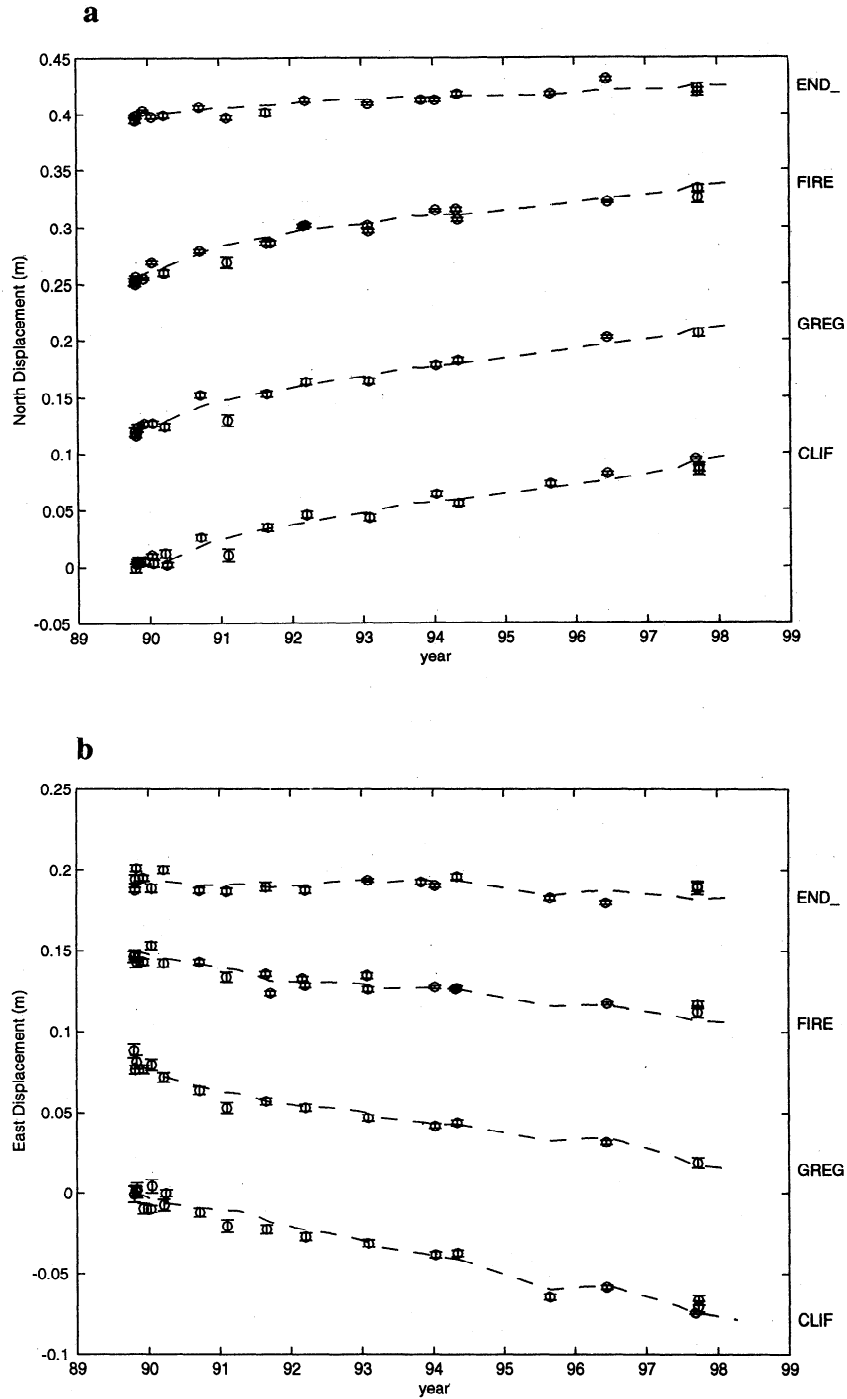
Figure 7. Observed (open circle with one standard deviation error bars) and predicted (dashed lines) displacements relative to station LP1 for selected sites southwest of LP1. (a) North component. (b) East component. Curves have been offset vertically for clarity.

eters are the following: (1) the three-dimensional position of all stations at the reference epoch t_0, the time of the first measurements following the earthquake, $x_r(t_0)$; (2) the slip rate coefficients $c_k(t)$ for both dip slip and strike slip on the two model faults at each measurement epoch; and (3) the three-dimensional random walk component of motion of all stations at each measurement epoch, $\mathcal{L}(x, t - t_0)$.

Results are shown in Figure 6 for $\tau = 0.003$ m/yr$^{1/2}$ and a temporal smoothing parameter α of 0.013 m/yr$^{3/2}$ Both components of slip decay with time on each of the faults, although not in a simple fashion. The Loma Prieta fault exhibits more dip slip postseismic motion than strike slip (Figure 6a). The strike slip component decays from an initial value of $\sim 3.0 \pm 1.0$ cm/yr to near zero by 1994. The reverse component of slip starts at

a

b

Figure 8. Observed (open circle with one standard deviation error bars) and predicted (dashed lines) displacements relative to station LP1 for selected sites northeast of LP1. (a) North component. (b) East component. Curves have been offset vertically for clarity.

5.7 ± 1.1 cm/yr immediately following the earthquake, decays to slightly more than 2 cm/yr by 1992, and then finally drops to near zero by 1994.

Slip on the Foothills thrust is nearly pure reverse slip. Although the strike-slip component is formally nonzero, we do not feel that this is significant. The reverse slip rate immediately after the mainshock was 4.5 ± 1.2 cm/yr, and this decayed to near zero by 1992 (Figure 6b). The oscillations in slip rate on the Foothills thrust following 1992 are most likely not significant, al-

though they are common features of multiple inversions.

It is important to recognize that the estimated postseismic rates of reverse slip are orders of magnitude greater than long-term geologic slip rates which are less than 1 mm/yr on the various faults [*McLaughlin and Clark*, 2000; *Bürgmann et al.*, 1994; *Anderson*, 1990; *Valensise and Ward*, 1991].

The model predictions are compared to the observations in Figures 7 and 8. In Figures 7 and 8 the predicted positions contain the secular trend $v_r^{sec}(x)$ and
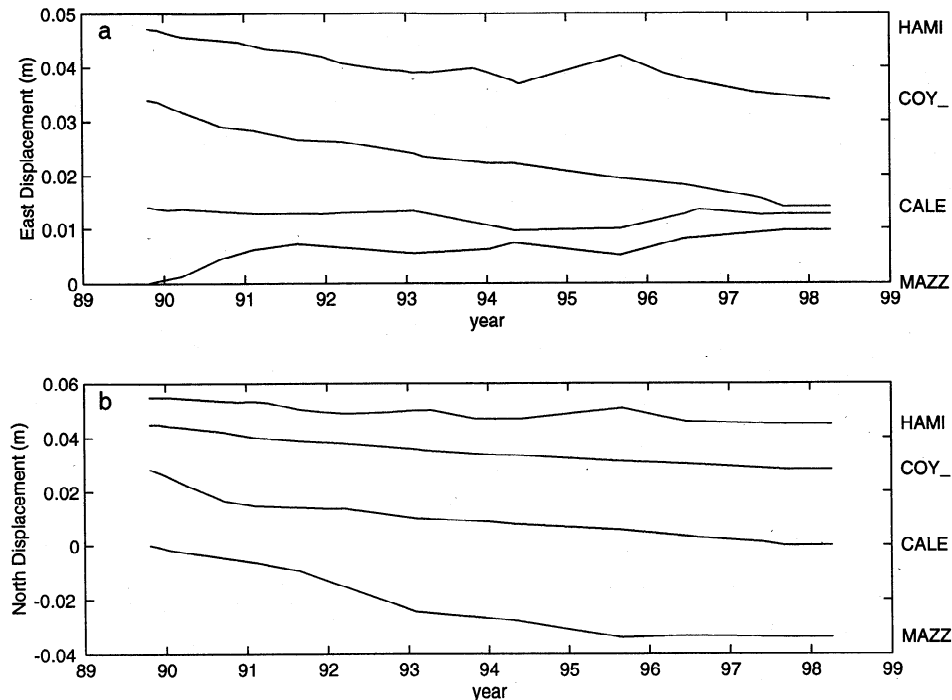
Figure 9. Random walk components of motion for selected sites northeast of the San Andreas fault. Curves have been offset vertically for clarity.
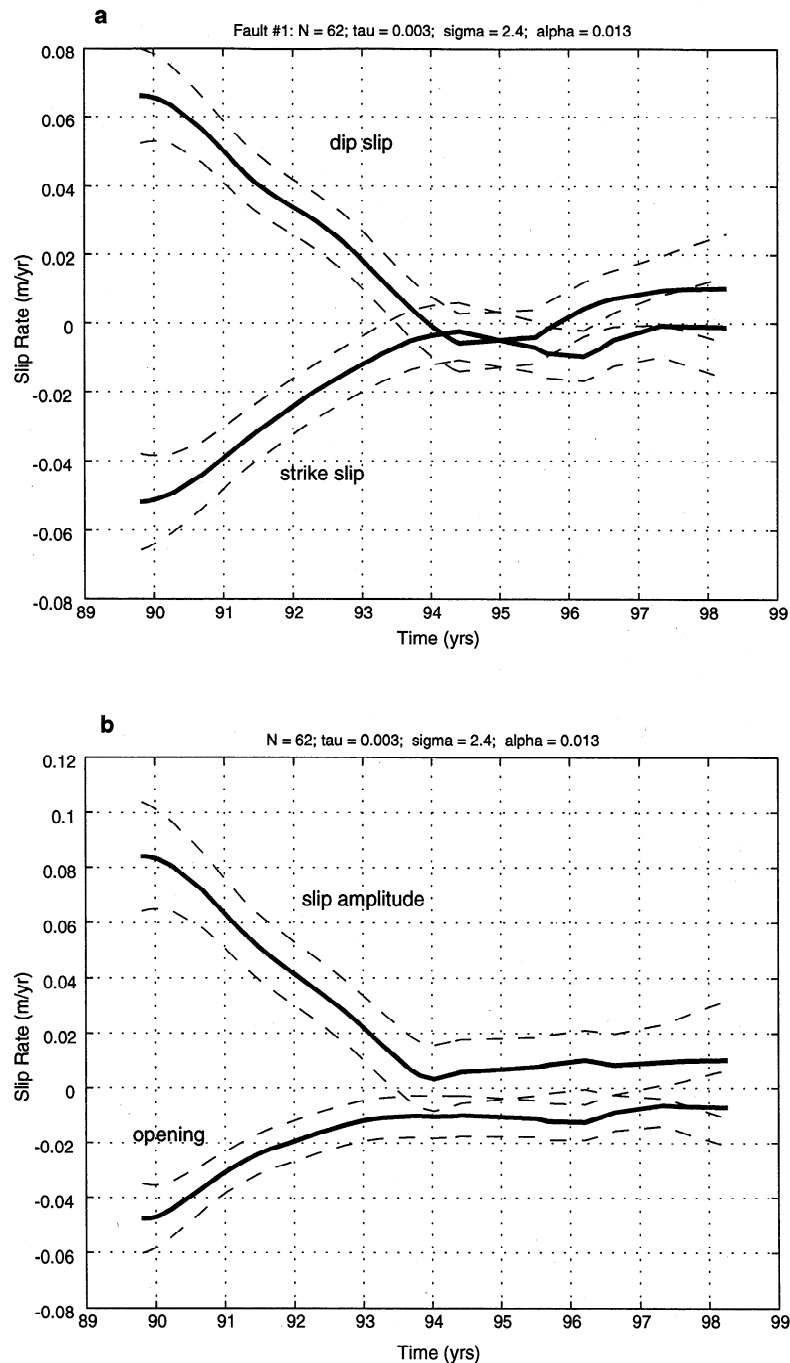
the estimated random walk components $\hat{\mathcal{L}}(\mathbf{x}, t - t_0)$, as well as the motion due to fault slip. The estimates of position at the reference epoch $\hat{\mathbf{x}}_r(t_0)$ and random walk $\hat{\mathcal{L}}(\mathbf{x}, t - t_0)$ are returned directly from the Kalman Filter. The estimated fault slip $\hat{s}_p(\boldsymbol{\xi}, t - t_0)$ is determined from equation (4). Because the positions of the benchmarks are estimated at the reference epoch, there is no arbitrary offset between the observed and predicted data in Figures 7 and 8 (observed and predicted values may be offset vertically by the same amount when plotted for clarity).

Although the slip model seems to do a reasonably good job of explaining the observations, there are indications that the model is not complete. The random walk components of motion alone show spatial correlations between nearby sites, which is inconsistent with our assumption that benchmark wobble is spatially incoherent. This correlation is illustrated for several sites northeast of the San Andreas fault in Figure 9. Here it can be observed that the north components of the random walk motion are all in the same direction at the sites HAMI, COY, CALE, and MAZZ. It is unlikely that this would occur randomly and suggests that there may be either missing sources of deformation or other limitations to the model explored here. For example, this may indicate that the observed convergence is accommodated on a more complex array of faults within the Foothills thrust belt.

We attempted to test *Savage et al.* 's [1994] hypothesis that the observed motions normal to the trend of the San Andreas are due to fault collapse. As in the

previous calculations, we assume spatially uniform slip and fault-perpendicular motion; however, slip on the Foothills thrust is excluded. The results shown in Figure 10 indicate that, assuming this explanation is correct, fault-normal collapse was roughly proportional to the amount of postseismic slip. The weighted residual sum of squares, $\mathbf{r}^T \Sigma^{-1} \mathbf{r}/N_{\text{obs}} = 3.38$, is slighlty greater than that found for the previous calculation, 3.35. We conclude that the GPS data alone can not distinguish between fault collapse on the mainshock rupture plane and fault-normal thrusting on the Foothills thrust system, consistent with the findings of *Bürgmann et al.* [1997]. The thrust faulting interpretation is supported by vertical displacements determined from leveling data, collected in 1990 and 1992 [*Bürgmann et al.*, 1997], compressional surface deformation observed along the Foothills thrust system following the Loma Prieta earthquake [*Langenheim et al.*, 1997], and a preponderance of reverse faulting aftershocks northeast of the San Andreas fault [*Bürgmann et al.*, 1997].

We also examined the possibility of deformation below the mainshock rupture plane. *Pollitz et al.* [1998] considered models that allow for postseismic fault slip as well as viscoelastic relaxation of the lower crust. They find that although most of the postseismic signal can be explained by fault slip, there is limited evidence for viscoelastic relaxation of the lower crust. *Linker and Rice* [1997] also considered finite element models of postseismic relaxation and stress transfer following the Loma Prieta earthquake. In this study we tested for time-dependent slip on a downdip extension of the

a

Fault #1: N = 62; tau = 0.003; sigma = 2.4; alpha = 0.013

[Figure 10a: Slip Rate (m/yr) vs Time (yrs), showing "dip slip" and "strike slip" curves with dashed standard deviation bounds]

b

N = 62; tau = 0.003; sigma = 2.4; alpha = 0.013

[Figure 10b: Slip Rate (m/yr) vs Time (yrs), showing "slip amplitude" and "opening" curves with dashed standard deviation bounds]

Figure 10. Estimated slip rate and fault opening rate, following the hypothesis of *Savage et al.* [1994]. (a) Strike slip and dip slip on the Loma Prieta fault as a function of time. Positive dip slip is thrust, right lateral strike slip is negative. (b) Slip amplitude and fault opening (negative values indicate collapse of the fault zone) as a function of time. Dashed lines indicate plus and minus one standard deviation bounds.

mainshock rupture plane. The deep fault segment is 8 km in downdip dimension, extending to a depth of 23 km. Slip on the deep fault segment could represent distributed deformation in a narrow zone or might very crudely represent more distributed flow in the lower crust. The Network Inversion Filter results for this geometry yielded significant deep slip; however the fit to the GPS data is not improved despite the increased model complexity. Dip slip decayed nearly linearly from

a rate of 5.1 ± 2.1 cm/yr to zero by 1994. Strike slip is never significant. There is no indication of a deep process with a longer decay time than that observed for slip on the mainshock rupture plane.

6. Spatially Variable Slip

We choose to start with a discrete basis set consisting of rectangular dislocations which tile the fault planes.

The displacements associated with each element are computed using the expressions of *Okada* [1985]. The discrete form of the observation equation (1) is

$$\mathbf{x}^* = \mathbf{x}_0 + \Gamma \mathbf{s} + \mathcal{L} + \epsilon. \tag{5}$$

Here $\mathbf{x}^*$ are the observed positions corrected for secular motion, $\mathbf{s}$ is a vector containing the slip magnitudes corresponding to each fault element, and Γ relates slip in each element to displacement. As solutions to (5) are, in general, nonunique, we seek solutions that fit the data and are reasonably smooth in the spatial domain. Spatial smoothing can be implemented in a number of ways [e.g., *Parker,* 1994; *Matthews and Segall,* 1993]. Here we seek solutions that minimize a roughness norm of the slip distribution $||T\mathbf{s}||$, where we take $T = \nabla^2$, a finite difference approximation to the Laplacian [*Harris and Segall,* 1987]. *Matthews* [1991] showed that the continuous analogue of this norm approximates a stress roughness norm.

The slip rate distribution can be expanded in some basis set $\mathcal{B}$,

$$\mathbf{s} = \mathcal{B}\mathbf{c}, \tag{6}$$

where $\mathbf{c}$ are time-varying coefficients and we postpone for the moment the particular choice of bases.

The observation equation (5) then becomes

$$\mathbf{x}^* = \mathbf{x}_0 + K\mathbf{c} + \mathcal{L} + \epsilon, \tag{7}$$

where $K = \Gamma\mathcal{B}$. The squared model norm is

$$||T\mathbf{s}||^2 = \mathbf{c}^T \mathcal{B}^T T^T T \mathcal{B}\mathbf{c}, \tag{8}$$

$$||T\mathbf{s}||^2 = \mathbf{c}^T \Psi E \Psi^T \mathbf{c}, \tag{9}$$

where E and Ψ are the eigenvalues and eigenvectors of $\mathcal{B}^T T^T T \mathcal{B}$. Note that from (9) the components corresponding to the basis functions with the largest eigenvalues contribute most to the roughness of the slip rate distribution. If there are multiple slip components, strike slip and dip slip, or multiple faults, then the squared model norm is the sum of contributions from each component.

Recall from (2) that the coefficients $\mathbf{c}$ have a steady state component v and an integrated random walk component $W(t)$. Written in state space form, the signal components of the state vector, $[v, W(t_k), \dot{W}(t_k)]^T$, the coefficients $c(t)$ are expressed as

$$c(t_k) = [t_k, 1, 0] \begin{bmatrix} v \\ W(t_k) \\ \dot{W}(t_k) \end{bmatrix}. \tag{10}$$

The state evolution equation corresponding to this model is given by *Segall and Matthews* [1997].

6.1. Smoothing Through A Priori State and Covariance

In the study by *Segall and Matthews* [1997] the amount of spatial smoothing was controlled by the a priori state
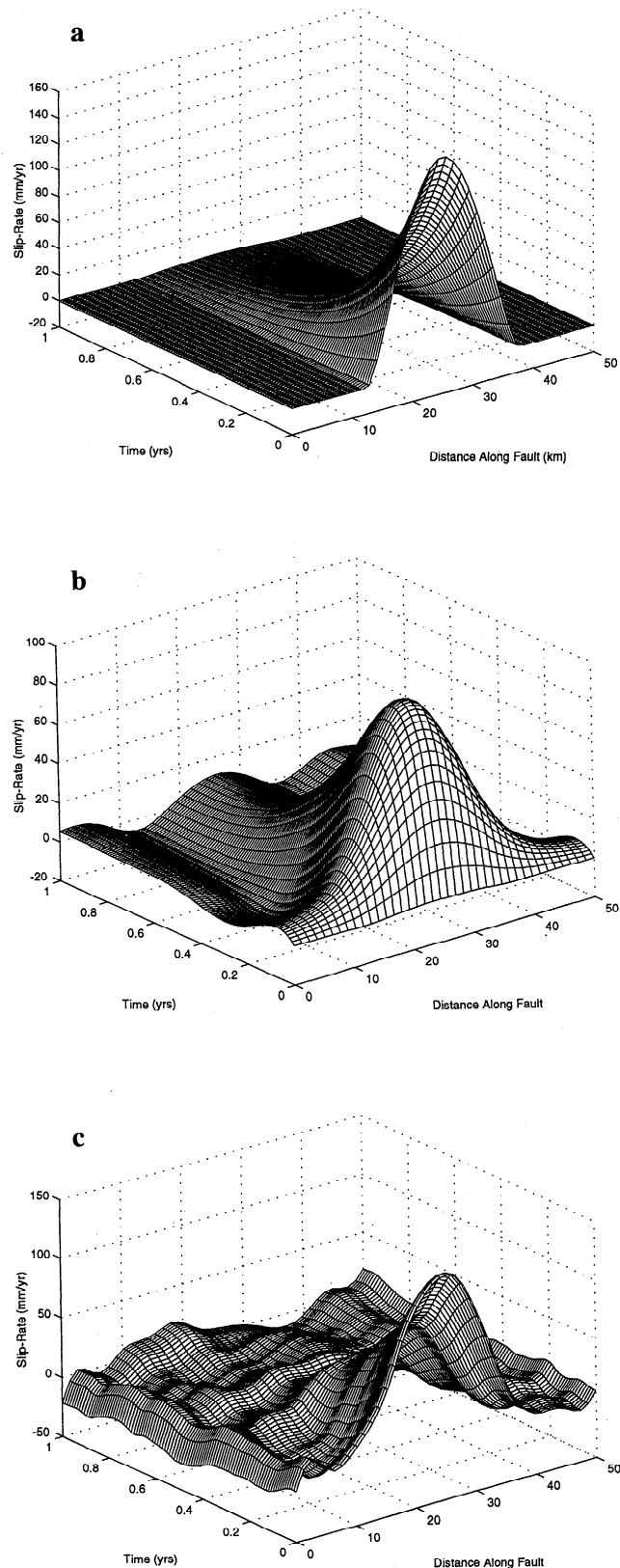
Figure 11. Simulation of decaying slip event on a horizontal fault. (a) True distribution of fault slip rate in space time. (b) Estimated slip rate with spatial smoothing imposed by the prior covariance matrix, as in the work of *Segall and Matthews* [1997], for $\gamma = 1$ and $\alpha = 100$. (c) Estimated slip rate with spatial smoothing imposed by pseudo-observations using the maximum likelihood estimates $\hat{\gamma} = 190.6$ and $\hat{\alpha} = 764.5$.

vector and its covariance. This procedure worked well with transient signals that increase with time but is not satisfactory for decaying transients such as postseismic slip. The reason for this is that imposing spatial smoothing through the prior state and covariance inexorably links the spatial and temporal domains. Specifically, in order for the solution to be spatially smooth, the transient component of the slip rate must be small at early times. This is clearly inappropriate for postseismic slip.

We illustrate this with a simulation of a decaying slip event on a horizontal fault. The problem is limited to two-dimensional, antiplane strain for simplicity. The true slip history is shown in Figure 11a. Synthetic data were generated for this event with added random walk ($\tau = 0.001$ m/yr$^{1/2}$) and white ($\sigma = 0.001$ m) noise. Basis functions were chosen in the following manner. Apply the simple transformation $\Gamma s = \Gamma T^{-1} T s = \Gamma' s'$ to the observation equation (5). From the singular value decomposition of $\Gamma' = U_p \Lambda_p V_p^T$, define basis functions

$$\mathcal{B} = T^{-1} V_p \Lambda_p^{-1}. \qquad (11)$$

The kernel K in the observation equation (7) is simply $K = U_p$. Also, $\Psi = I$ and $E = \Lambda^{-2}$. From (9), note that the components corresponding to the smallest singular values contribute most to the roughness of the slip distribution.

With this approach spatial smoothing is implemented by setting the a priori value of the coefficients $\mathbf{c}$ to zero. The a priori variances scale with Λ^2, so that coefficients corresponding to large singular values are only weakly constrained to zero, whereas terms corresponding to small singular values are tightly constrained to zero.

Employing the methods described by *Segall and Matthews* [1997], we determine maximum likelihood estimates of the spatial and temporal smoothing parameters of $\gamma = 107$ and $\alpha = 662$. This resulted in an estimated slip rate distribution that was quite oscillatory in the spatial domain. While decreasing γ leads to a smoother slip rate distribution it also forces the initial slip rate to zero (Figure 11b). This is clearly an unsatisfactory fit to the initial input slip rate distribution (Figure 11a), motivating us to explore alternative methods for smoothing that decouple the spatial and temporal domains.

6.2. Smoothing Through Pseudo-Observations

In order to separate the spatial and temporal domains, we impose spatial smoothing at each time step in the Kalman Filter. To do so, we augment the observation equations with pseudo-observations.

The state vector for the full geodetic network is

$$\begin{aligned}
\mathcal{X}_k = & [v_1, W_1(t_k), \dot{W}_1(t_k), v_2, W_2(t_k), \dot{W}_2(t_k), \\
& \dots v_M, W_M(t_k), \dot{W}_M(t_k), \\
& B_1(t_k), B_2(t_k), \dots B_N(t_k), \\
& \mathbf{x}_1(t_0), \mathbf{x}_2(t_0), \dots \mathbf{x}_N(t_0)]^T, \qquad (12)
\end{aligned}$$

where M is the number of basis functions and N is the number of data (3 times the number of stations in the network). The first group of terms, $\dots v_M, W_M(t_k), \dot{W}_M(t_k) \dots$, are related to the coefficients of fault slip, as in (10). The second set of terms, $\dots B_N(t_k) \dots$, represent the Brownian motion for all the stations at epoch k. The final set of terms, $\dots \mathbf{x}_N(t_0) \dots$, correspond to the coordinates of the stations at the initial epoch. The length of the state vector is $3M + 2N$; three terms for each basis vector, one term for the random walk component at each station, and one term for the initial coordinates of each station.

The observation equations are

$$\mathbf{d}_k = H_k \mathcal{X}_k + \epsilon_k \qquad \epsilon_k \sim N(\mathbf{0}, \sigma^2 \Sigma), \qquad (13)$$

where $\mathbf{d}_k$ and $\mathcal{X}_k$ represent the data and state vector at epoch $t_k, k = 0, 1, 2, \dots N_{\text{epochs}}$. The second part of (13) signifies that the observation errors ϵ_k are assumed to be normally distributed with zero mean and covariance $\sigma^2 \Sigma$. The matrix H_k relates the data to the state vector and is given by *Segall and Matthews* [1997].

Recall from (9) that the squared spatial roughness norm is given by $||Ts||^2 = \mathbf{c}^T \Psi E \Psi^T \mathbf{c}$. Thus equations of the form $\mathbf{0} = E^{1/2} \Psi^T \mathbf{c}$ enforce the prior expectation that the roughness of the fault slip distribution is small (near zero). We introduce such "pseudo-observations" at each epoch of the Kalman Filter

$$\mathbf{0} = E^{1/2} \Psi^T [A_k \ \mathbf{0}] \mathcal{X}_k + \omega_k \qquad \omega_k \sim N(\mathbf{0}, \gamma^2 I), \quad (14)$$

where the matrix A_k maps the state vector to the coefficients $\mathbf{c}_k$ and is given by

$$A_k = \begin{bmatrix} t_k & 1 & 0 & 0 & 0 & 0 & 0 \\ 0 & 0 & 0 & t_k & 1 & 0 & 0 \\ 0 & 0 & 0 & 0 & 0 & 0 & t_k \\ & & & & & & & \ddots \end{bmatrix}. \qquad (15)$$

The pseudo-observations have mean zero and variance γ^2. Note that A_k has dimension Nbasis × 3Nbasis, where Nbasis is the number of basis functions. The zero vector $\mathbf{0}$ in (14) annihilates the components of the state vector associated with random benchmark motion and initial coordinates. The equations (14) act to keep the coefficients $\mathbf{c}_k$ small, depending on the size of the associated eigenvalue. Large eigenvalues, associated with basis functions that contribute most to the spatial roughness, are more heavily weighted than small eigenvalues.

The observation equations (13) and the pseudo-observations (14) can be written together

$$\begin{bmatrix} \mathbf{d}_k \\ \mathbf{0} \end{bmatrix} = \begin{bmatrix} H_k \\ S_k \end{bmatrix} \mathcal{X}_k + \delta_k, \qquad (16)$$

where the smoothing matrix S_k is given by

$$S_k = [E^{1/2} \Psi^T A_k, \ \mathbf{0}]. \qquad (17)$$

The errors δ_k are distributed as $N(\mathbf{0}, R_k)$, where

$$R_k = \begin{pmatrix} \sigma^2\Sigma & 0 \\ 0 & \gamma^2 I \end{pmatrix}. \qquad (18)$$

It should be clear that the the observation equations and pseudo-observation equations can not be satisfied exactly. Equation (16) is solved by weighted least squares, via Kalman Filtering, with the covariance matrix (18). The ratio γ^2/σ^2 weights the relative importance of minimizing the solution roughness versus fitting the observations $\mathbf{d}_k$. As γ^2/σ^2 is reduced, the solution becomes smoother in the spatial domain, whereas increasing γ^2/σ^2 allows the model to fit the data more accurately.

We tested the modified Network Inversion Filter using spatial smoothing at each epoch on the simulation shown in Figure 11a. For the previous choice of basis functions $E^{1/2}\Psi^T = \Lambda^{-1}$. The maximum likelihood analysis returned estimates of spatial and temporal smoothing parameters of $\hat{\gamma} = 193.8$ and $\hat{\alpha} = 777.4$. The estimated white noise standard deviation $\hat{\sigma}$ was 1.004, very close to the true value of 1.0. To simplify the analysis, we employed the true value of τ, 0.001 m/yr$^{1/2}$. *Segall and Matthews* [1997] showed that, given enough data, maximum likelihood employing the Network Inversion Filter leads to reasonable estimates of the random walk scale parameter.

The estimated slip rate distribution in space and time using the maximum likelihood estimates of the spatial and temporal smoothing parameters is shown in Figure 11c. Notice that the estimated slip rate at $t = 0$ is a maximum and decays with increasing time as does the true slip rate (Figure 11a). Although the estimated slip rate distribution contains short-wavelength spatial roughness, it reasonably approximates the true input slip rate. In addition, increasing the amount of spatial smoothing, by decreasing γ, does not force the initial slip rate toward zero, as in Figure 11b. We conclude that smoothing at each filter epoch using pseudo-observations allows for the detection of decaying transient deformations.

6.3. Application to Loma Prieta Postseismic Slip

We start with the observation equation (5). A reasonable approach would be to choose basis functions as in (11). This basis, however, does not have the property that the slip distribution becomes uniform in the limit that $\gamma \to 0$. We would like to test for resolvable spatial nonuniformity in the same fashion that we previously tested for nonsteady behavior. To do so requires that the slip becomes uniform in the limit $\gamma \to 0$. To include this property, we choose the first basis function
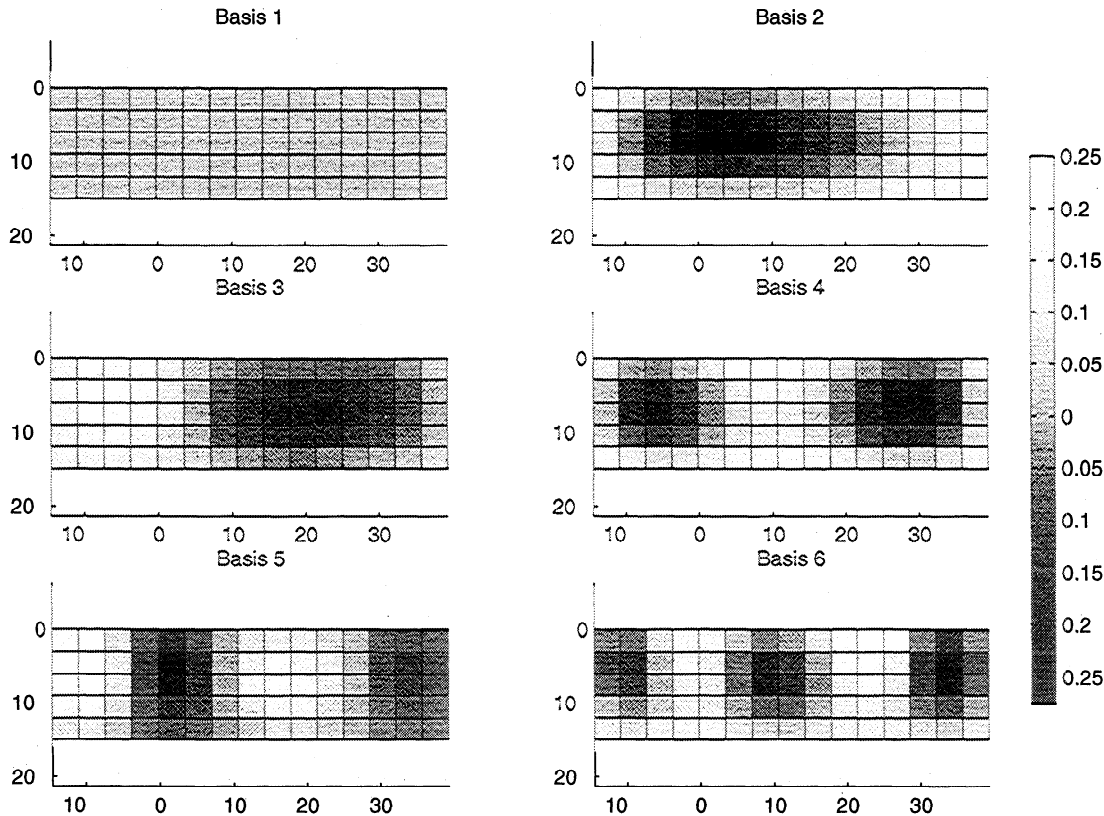
Figure 12. Spatial basis functions for strike slip on the Loma Prieta Fault. Each subplot shows the fault looking from the SW. Depth and along-strike distance are in kilometers. The estimated slip rate distribution is a linear combination of these functions, with coefficients that vary in time such as to fit the GPS data.

for each slip component to be uniform, and we then choose the remaining basis functions from the set (11) such that $\mathcal{B}_i$ are orthonormal using Gram-Schmitt orthogonalization. This produces a basis set $\mathcal{B}$ that is locally orthonormal; i.e., $\mathcal{B}^T\mathcal{B} = I$ if we consider only the components of $\mathcal{B}$ associated with each component of slip on each fault. The spatial basis functions are shown for strike slip on the Loma Prieta fault in Figure 12. Dip-slip bases on the Loma Prieta fault and Foothills thrust are similar. The kernel K in the observation equation (7) is then given by $K = \Gamma\mathcal{B}$.

We now follow the procedure outlined in section 6.2, except that there are now only Nbasis -1 pseudo-observations, and A_k is modified so that the first coefficient c_1 for each component, corresponding to uniform slip, is annihilated,

$$
A_k = \begin{bmatrix} 0 & 0 & 0 & t_k & 1 & 0 & 0 & 0 & 0 & 0 & 0 & 0 \\ 0 & 0 & 0 & 0 & 0 & 0 & t_k & 1 & 0 & 0 & 0 & 0 \\ 0 & 0 & 0 & 0 & 0 & 0 & 0 & 0 & 0 & t_k & 1 & 0 \\ & & & & & & & & & & & \ddots \end{bmatrix},
$$

(19)

so that A_k now has dimension Nbasis-1 $\times$ 3Nbasis. The limit that $\gamma \rightarrow 0$ ensures that the coefficients corresponding to the nonuniform slip basis functions are set to zero. Nonzero γ allows the slip distribution to vary spatially in order to better fit the observations. We have verified that in the limit $\gamma \rightarrow 0$, the previous uniform slip results were recovered.

Maximum likelihood estimates of spatial and temporal smoothing parameters followed the procedure described by *Segall and Matthews* [1997]. The component of the residual vector, or "innovations" associated with the pseudo-observations, and the associated covariance are not included in the likelihood calculation. In this way the likelihood reflects only the fit to the GPS data not the smoothing constraints.

We judged it important to conduct the maximum likelihood analysis using as much data as possible. This makes the computations quite time intensive. We limited the number of basis functions to six for each fault slip component. Allowing for strike slip and dip slip on the Loma Prieta fault and dip slip on the Foothills thrust fault, there are a total of 18 basis functions. A coarse grid search in (α, γ) space, involving eight values of the temporal smoothing parameter and six values of the spatial smoothing parameter, with the random walk parameter $\tau = 0.003$ m/yr$^{1/2}$ consumed $\sim$ 7 Terraflops, which is a limit of what is feasible on a workstation. The minus twice the likelihood surface does exhibit a minimum over the tested range (Figure 13). The likelihood for the full data set is maximized at $\hat{\alpha} = 0.066$, $\hat{\gamma} = 5.5 \times 10^{-5}$, and $\hat{\sigma} = 3.45$.

An advantage of the present formulation is that we can use the likelihood difference to test the significance
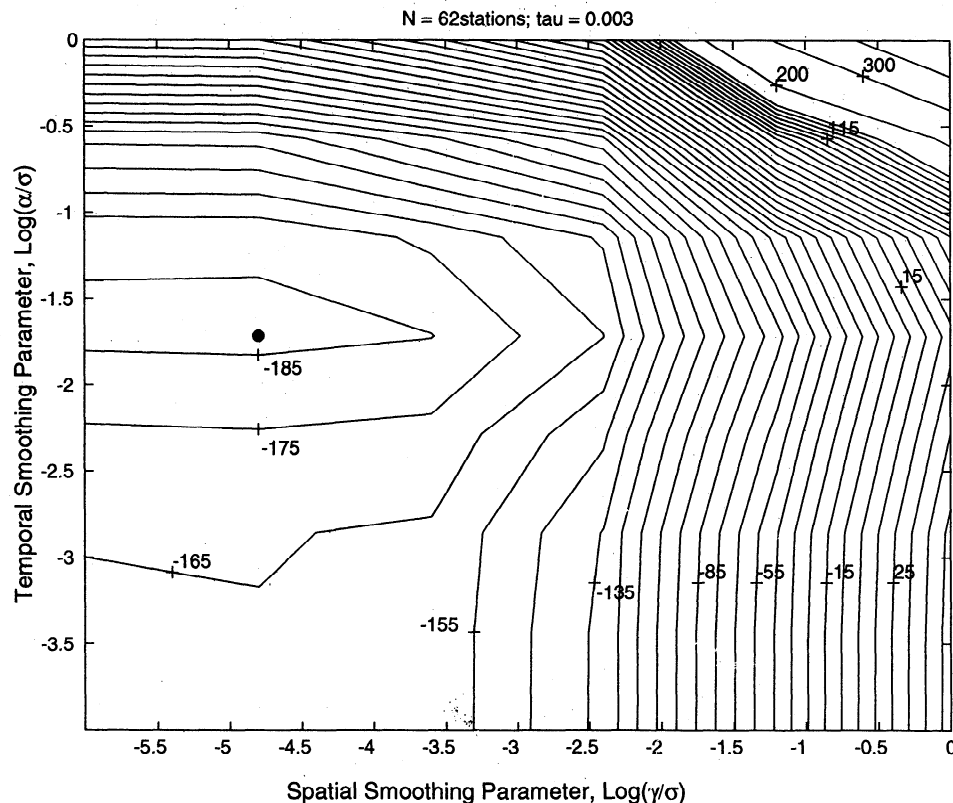
Figure 13. Maximum likelihood analysis used to determine spatial smoothing parameter for the full data set. Minus twice the logarithm of the likelihood surface as a function of $log_{10}(\alpha/\sigma)$ and $log_{10}(\gamma/\sigma)$. The maximum likelihood estimate is indicated by an asterisk.

of the spatially nonuniform solution. We compare the loglikelihood at the maximum likelihood point, L_{ml}, with the likelihood when γ is constrained to be zero, L_0 (in practice we use the smallest value of γ tested, as an approximation for zero). This test parallels the test for nonsteady behavior in section 4. For $L_{ml} = 93.821$ and $L_0 = 93.578$ the likelihood difference statistic is $2(L_{ml} - L_0) = 0.486$. This value corresponds to the 51% point of the cummulative χ^2 distribution with one degree of freedom, suggesting that spatial variations are not resolved by the data.

Even if we adopt the maximum likelihood estimate of γ as significant, $\hat{\gamma}$ itself is small, and slip distributions corresponding to the maximum likelihood values of the parameters are nearly spatially uniform. For the Loma Prieta fault the maximum deviation from uniform slip is 2 mm/yr. For dip slip motion on the Foothills thrust the maximum observed deviation is 2.4 mm/yr. While it is certainly possible, indeed likely, that fault slip was more spatially variable than this, it could not be resolved with the present data set. The fit to the data with modest spatially variable slip is not distinguishable from the uniform slip results (Figures 7 and 8).

7. Discussion

We have concluded that spatial variations in postseismic slip are not well resolved by the GPS data, in contrast to the conclusion of *Pollitz et al.* [1998] who estimated spatially variable slip on the Loma Prieta and Foothills faults. Pollitz et al. ignored temporal variations in deformation and modeled the average station velocities from 1989 to 1994. Uncertainties in the average velocities due to random benchmark motions were approximated by adding a small component to the velocity covariance matrix. Some postseismic leveling data were included, as were the effects of lower crustal relaxation, although the latter was not found to be a first-order feature of the data. In contrast, we solve for the spatial and temporal variations simultaneously and explicitly include the effects of random benchmark motion in the observed time series. If Pollitz et al. underestimate the true uncertainties in the site velocities, they may have overestimated the spatial resolution of the data. On the other hand, we do not model lower crustal relaxation in our calculations.

In order to test whether our inability to resolve spatial variability in slip is related to the improved temporal resolution, we explored inversions constrained to steady state ($\alpha = 0$). The random walk scale was fixed to $\tau = 0.003$ m/yr$^{1/2}$. The maximum likelihood estimate of the spatial smoothing parameter for this case lies in the range $5 \times 10^{-5} < \hat{\gamma} < 6 \times 10^{-3}$. The shape of the likelihood surface (Figure 13) emphasizes that allowing for spatial variability makes for a small change in the likelihood, whereas allowing for temporal variablity makes a significant change in the likelihood. This confirms that temporal variation is much better resolved by the data than is spatial variation.

The estimated, steady state slip rate distributions for $\alpha = 0$ and $\hat{\gamma} = 0.001$ (not shown) bear some resemblance to those found by *Pollitz et al.* [1998], although the amplitudes of the slip variations are much smaller. This is presumably because we choose the first basis function to be uniform slip and determine the amount of spatial smoothing by maximum likelihood. We find a weak dipolar pattern in the slip distributions, indicating that only the first three basis functions are contributing to the solution. The dip slip rate on the Loma Prieta fault is higher on the southeastern half of the fault (21 mm/yr maximum) in comparison to the northwestern half (12 mm/yr minimum). Pollitz et al. find a more complex but crudely similar pattern with variations from ~ 35 mm/yr to as low as ~ 5 mm/yr. Similarly, for the strike-slip component the estimated slip rate is slightly higher in the southeast, but the difference is < 1 mm/yr. Pollitz et al. find spatial variations of more than 20 mm/yr. For the Foothills thrust we find 4 mm/yr more reverse slip in the northwestern half of the fault. To reiterate, while we find hints of the same spatial slip rate patterns as those observed by Pollitz *et al.*, we conclude that spatial variations in slip rate are weakly resolved, particularly in comparison to temporal variations.

Figure 14a shows the average velocities over three time periods: 1989.8-1991.75, 1991.75-1994.25, and 1994.25-1996.65, relative to Mount Hamilton (station HAMI). Vectors are shown only for the time periods for which the data reasonably well constrain the velocity. It is apparent from Figure 14a that most of the anomalous fault-perpendicular motion occurred in the first 2 years after the earthquake. The corresponding velocity field predicted by the time-dependent slip model (spatially uniform slip) is shown in Figure 14b. Here vectors are plotted at all stations for each of the three time periods. It appears that the time-varying slip model does a reasonably good job of describing the observed motions.

Evidence discussed by *Bürgmann et al.* [1997] suggests that the San Andreas normal motion observed following the Loma Prieta earthquake was related to slip on one or more faults in the Foothill thrust belt. Postseismic leveling data are somewhat better fit with this model than with fault collapse on the 1989 mainshock plane. Further support comes from compressional surface deformation and numerous reverse faulting aftershocks observed following the Loma Prieta earthquake. Modeling the Foothills thrust belt faults as a single, elastic dislocation undoubtedly oversimplifies the mechanics of the postseismic process. Nevertheless, the data and present analysis support the conclusion that triggered afterslip occurred off the main rupture zone on adjacent faults. The analysis also suggests that afterslip on the Foothills thrust decayed more rapidly than afterslip on the Loma Prieta rupture did.

Our results support previous studies that concluded that shallow afterslip (as opposed to distributed lower crustal relaxation) dominated the postseismic deformation field for the first 5 years after the 1989 earthquake.
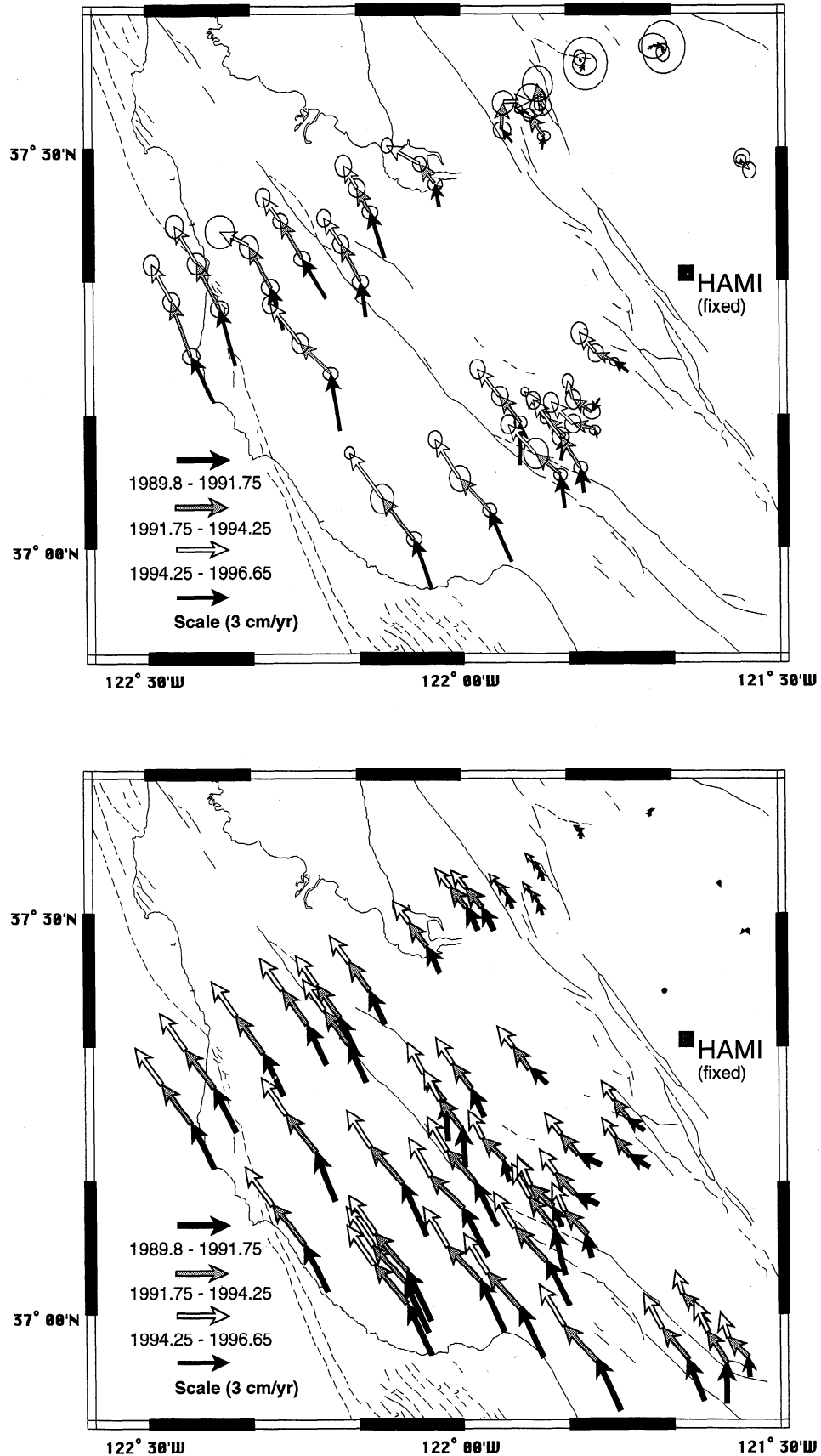
Figure 14. Time-dependent velocity field. (a) Observed station velocities for three time periods. Error ellipses are 68% confidence regions. (b) Predicted station velocities from spatially uniform slip model. Note that predicted velocities are computed at all sites, whereas observed velocities are only shown at sites for which data are available.

We suggest that the bulk of the afterslip had decayed by 1994. It is thus possible to search for deeper-seated processes in the data collected after 1994. It should be noted, however, that the interseismic deformation field in this region is not well constrained. It will thus be difficult to distinguish effects of lower crustal relaxation from errors in the assumed pre-earthquake deformation field. With sufficient data it may be possible to detect time-dependent deformation with time constants much longer than the few years exhibited by afterslip.

Our time-dependent fault slip model suggests that during the first 3 years after the earthquake, $\sim$ 92 mm of dip slip occurred along a 50 km long segment of the Foothills thrust system. Thus aseismic slip released a moment of 1.5×10^{18} N-m, equivalent to a $M_w = 6.1$ earthquake. In addition, significant ground deformation along the surface trace of the thrust system was observed following the Loma Prieta earthquake [*Langenheim et al.*, 1997], suggesting triggered slip at least on the shallow portions of the thrusts. Similar damage patterns were observed following the 1906 San Francisco earthquake [*Lawson*, 1908]. Apparently, several centimeters of triggered and postseismic creep on the Foothills thrusts are associated with nearby major earthquakes. The repeat time of a potential $M_w = 6.8$ thrust event along the Monte Vista thrust fault has been estimated at 2400 years, corresponding to a seismic moment rate of 7×10^{15} N-m/yr and a geologic slip rate of 0.4 mm/yr [*Working Group on Northern California Earthquake Potential*, 1996]. Aseismic thrusting alone, as observed by repeated GPS measurements over a 3 year period, may thus have released $\sim$ 220 years of elastic strain accumulation. Triggered slip during Loma Prieta type events and large earthquakes along the San Andreas fault, which occur every few hundred years, account for an even larger amount of moment release. Thus a significant amount of the active thrusting along the Santa Clara Valley may be accommodated by aseismic processes. This finding likely reduces the estimate of earthquake hazards from the thrust faults. However, only more detailed descriptions of the distribution of aseismic slip and careful paleoseismic observations will clarify the distribution of aseismic and seismic slip along the Foothills thrusts. It is possible that segments along the thrust belt did not participate in the sympathetic coseismic slip and have actually experienced significant loading during and in the aftermath of the Loma Prieta earthquake. Postseismic afterslip on the Loma Prieta rupture through 1994 amounted to $\sim$ 67 mm of right-lateral strike slip and $\sim$ 138 mm of dip slip, equivalent to a moment of 3.6×10^{18} N-m. Afterslip thus contributed an additional 10% of the coseismic moment, which was estimated at $\sim$ 3.0 to 3.5 $\times 10^{19}$ N-m in seismic and geodetic studies [e.g., *Árnadóttir and Segall*, 1994]. Significant afterslip also followed other recent California earthquakes, suggesting that estimates of moment release used in earthquake potential estimates should account for additional postseismic slip.

8. Conclusions

We have presented time-dependent inversion techniques capable of imaging the spatiotemporal history of postseismic slip. Methods are presented for testing the significance of both spatial and temporal changes in slip rate. GPS data collected in the 8 years following the 1989 Loma Prieta earthquake reveal decaying slip rates on the mainshock fault plane and triggered afterslip on thrust fault(s) northeast of the San Andreas. Slip rate on the adjacent thrust appears to decay more rapidly than does slip on the Loma Prieta rupture plane. Spatial variations in slip rate are not well resolved by the data. Postseismic deformation data with higher signal-to-noise ratio than that available for this study should allow the space-time evolution of afterslip to be resolved. Shallow afterslip dominates postseismic deformation in the first 8 years after the Loma Prieta earthquake.

References

Aki, K., and P.G. Richards, *Quantitative Seismology: Theory and Methods*, 932 pp., W. H. Freeman, New York, 1980.

Anderson, R. S., Evolution of the northern Santa Cruz Mountains by advection of crust past a San Andreas fault bend, *Science, 249*, 397-401, 1990.

Árnadóttir, T., and P. Segall, The 1989 Loma Prieta earthquake imaged from inversion of geodetic data, *J. Geophys. Res., 99*, 21,835-21,855, 1994.

Bennett, R.A., R.E. Reilinger, W. Rodi, Y. Li, M.N. Toksöz, and K. Hudnut, Coseismic fault slip associated with the 1992 M_w 6.1 Joshua Tree, California, earthquake: Implications for the Joshua Tree-Landers earthquake sequence, *J. Geophys. Res. 100*, 6,443-6,461, 1995.

Beutler, G., M. Rothacher, T. Springer, J. Kouba, R.E. Neilan, International GPS Service (IGS): An Interdisciplinary Service in Support of Earth Sciences, *32nd COSPAR Scientic Assembly*, Nagoya, Japan, 1998.

Bilham, R., Surface slip subsequent to the 24 November 1987 Superstition Hills, California, earthquake monitored by digital creepmeters, *Bull. Seismol. Soc. Am., 79*, 424-450, 1989.

Bürgmann, R., R. Arrowsmith, T. Dumitru, and R. McLaughlin, Rise and fall of the southern Santa Cruz Mountains, California, deduced from fission track dating, geomorphic analysis, and geodetic data, *J. Geophys. Res., 99*, 20,181- 20,202, 1994.

Bürgmann, R., P. Segall, M. Lisowski, and J.P. Svarc, Postseismic strain following the 1989 Loma Prieta earthquake from repeated GPS and leveling measurements, *J. Geophys. Res., 102*, 4,933-4,955, 1997.

Harris, R., and P. Segall, Detection of a locked zone at depth on the Parkfield, California segment of the San Andreas fault, *J. Geophys. Res., 92*, 7,945-7,962, 1987.

Heki, K., S. Miyazaki, H. Tsuji, Silent fault slip following an

interplate thrust earthquake at the Japan Trench, *Nature* *386*, 595-598, 1997.

Hudnut, K.W., et al., Co-seismic displacements of the 1992 Landers earthquake sequence, *Bull. Seismol. Soc. Am.*, *84*, 625-645, 1994.

King, N. E., J. L. Svarc, E. B. Fogelman, W. K.Gross, K. W. Clark, G. D. Hamilton, C. H. Stiffler, J. M. Sutton, Continuous GPS observations across the Hayward Fault, California, 1991-1994, *J. Geophys. Res.*, *100*, 20,271-20,283, 1995.

Langbein, J., and H. Johnson, Correlated errors in geodetic time series: implications for time-dependent deformation, *J. Geophys. Res.*, *102*, 591-603, 1997.

Langenheim, V.E., K.M. Schmidt, and R.C. Jachens, Co-seismic deformation during the 1989 Loma Prieta earthquake and range-front thrusting along the southwestern margin of the Santa Clara Valley, California, *Geology, 25*, 1091-1094, 1997.

Larson, K. M., F. H. Webb, and D. C. Agnew, Application of the Global Positioning System to crustal deformation measurement, 1, Precision and accuracy, *J. Geophys. Res.*, *96*, 16,547-16,565, 1991.

Lawson, A. C. (Ed.), *The California Earthquake of April 18, 1906, Report of the State Earthquake Investigation Commission*, vol. 1, Carnegie Inst. of Wash., Washington, D.C., 1908.

Linker, M.F., and J.R. Rice, Models of postseismic deformation and stress transfer associated with the 1989 Loma Prieta, California, earthquake, *U.S. Geol. Surv. Prof. Pap., 1550-D*, 253-275, 1997.

Matthews, M. V., On the estimation of fault slip in space and time, Ph.D. thesis, 241 pp., Stanford Univ., Stanford Calif., 1991.

Matthews, M. V., and P. Segall, Detecting transient fault slip with frequently sampled deformation measurements (abstract) *Eos, Trans. AGU, 69*(44), p. 1432, 1988.

Matthews, M. V., and P. Segall, Statistical inversion of crustal deformation data and estimation of the depth distribution of slip in the 1906 earthquake, *J. Geophys. Res.*, *98*, 12,153–12,163, 1993.

McLaughlin, R. J., and E. E. Clark, Stratigraphy and structure of rocks across the San Andreas fault zone near Loma Prieta, California: Their relation to deformation during the October 17, 1989 earthquake, in *The Loma Prieta, California Earthquake of October 17, 1989-Geologic Setting and Crustal Structure* U.S. Geol. Surv. Prof. Pap., 1550-E, in press, 2000.

Menke, W., *Geophysical Data Analysis: Discrete Inverse Theory*, 260 pp., Academic Press, Inc. San Diego, Calif., 1984.

Murray M., G.A. Marshall, M. Lisowski, R.S. Stein, The 1992 M=7 Cape Mendocino, California, Earthquake: Co-seismic deformation at the south end of the Cascadia megathrust, *J. Geophys. Res.*, *101*, 17,707-25, 1996.

Okada, Y., Surface deformation due to shear and tensile faults in a half-space, *Bull. Seismol. Soc. Am.*, *75*, 1135–1154, 1985.

Parker, R.L., *Geophysical Inverse Theory*, 386 pp., Princeton University Press, Princeton, N.J., 1994.

Pollitz, F., R. Bürgmann, and P. Segall, Joint estimation of afterslip rate and postseismic relaxation following the 1989 Loma Prieta earthquake, *J. Geophys. Res.*, *103*, 26,975-26,992, 1998.

Prescott, W.H., N.E. King, and G. Guohua, Preseismic, coseismic, and postseismic deformation associated with the 1984 Morgan Hill, Calif. earthquake, *Spec. Publ. Calif. Div. Mines Geol. 68*, 137-148, 1984.

Rothacher, M., and L. Mervart, (Eds.) *Documentation of the Bernese GPS Software Version 4.0*, 418 pp., Astron. Inst., Univ. of Berne, Berne, Switzerland, 1996.

Savage ,J.C. and J. L. Svarc, Postseismic deformation associated with the 1992 $M_W = 7.3$ Landers earthquake, southern California, *J. Geophys. Res.*, *102*, 7565-7577, 1997.

Savage, J.C., M. Lisowski, J. and L. Svarc, Postseismic deformation following the 1989 (M= 7.1) Loma Prieta, California, earthquake, *J. Geophys. Res.*, *99*, 13,757-13,765,1994.

Segall, P., and M. Matthews, Time dependent inversion of geodetic data, *J. Geophys. Res.*, *102*, 22,391-22,400., 1997.

Shen Z.K., D.D. Jackson, Y. Feng , M. Cline, M. Kim, P. Fang, and Y. Bock, Postseismic deformation following the Landers earthquake, California, 28 June 1992, *Bull. Seismol. Soc. Am.*, *84*, 780-791, 1994.

Smith, S.W., and M. Wyss, Displacement on the San Andreas fault subsequent to the 1966 Parkfield earthquake, *Bull. Seismol. Soc. Am.*, *58*, 1955-1973, 1968.

Valensise, G., and S. N. Ward, Long-term uplift of the Santa Cruz coastline in response to repeated earthquakes along the San Andreas fault, *Bull. Seism. Soc. Am.*, *81*, 1694-1704, 1991.

Wald, D. J., and T. H. Heaton, Spatial and temporal distribution of slip for the 1992 Landers, California, earthquake, *Bull. Seismol. Soc. Am.*, *84*, 668-691, 1994.

Working Group on Northern California Earthquake Potential, Database of potential sources for earthquakes larger than magnitude 6 in northern California, *U.S. Geological Survey Open File Rep.*, 96-705, 1996.

Wyatt, F. K., Displacement of surface monuments: horizontal motion, *J. Geophys. Res.*, *87*, 979-989, 1982.

Wyatt, F. K., Displacement of surface monuments: vertical motion, *J. Geophys. Res.*, *94*, 1,655-1,664, 1989.

R. Bürgmann, Department of Geology and Geophysics, University of California Berkeley, Berkeley, CA 94720.

M. Matthews, Walden Consulting, 143 Concord Road, Wayland, MA 01778.

P. Segall, Department of Geophysics, Stanford University, Stanford, CA 94305. (segall@stanford.edu)